Aerospace Science and Technology 128 (2022) 107746

Contents lists available at ScienceDirect

Aerospace Science and Technology

www.elsevier.com/locate/aescte

System energy benefit using co-flow jet active separation control for a serpentine duct

Kewei Xu, Gecheng Zha *

Department of Mechanical and Aerospace Engineering, University of Miami, Coral Gables, FL 33124, USA

A R T I C L E   I N F O

Article history:
Received 16 April 2022
Received in revised form 26 June 2022
Accepted 5 July 2022
Available online 13 July 2022
Communicated by Mehdi Ghoreyshi

Keywords:
CoFlow jet active flow control
Energy benefit
Exergy analysis
Serpentine duct
Separation elimination

A B S T R A C T

Even though active flow control has attracted broad interest to improve flow performance by adding external energy, few studies investigate whether the energy consumed by the AFC can bring energy benefit to the system. This paper numerically demonstrates that co-flow jet (CFJ) active flow control can not only eliminate the flow separation and distortion of a serpentine duct (S-duct), but also leverage the energy state of the inlet system with the available work increased more than the CFJ energy consumed. The 3D Reynolds Averaged Navier-Stokes (RANS) equations with one-equation Spalart-Allmaras turbulence model are used and validated with experiments for the simulation. The optimum configuration of the CFJ S-duct removes the flow separation and virtually eliminates the distortion by reducing DC_{60} from 41.7% to 0.67%. Benefited from the attached flow, the total pressure recovery is increased by 2.0%. An exergy analysis is conducted to assess the potential benefit of the system available work. A parameter, $EIPR$, is introduced to measure the merit of an AFC by calculating the ratio of exergy increase to the power required by the AFC. Attributed to the zero-net-mass-flux control, all the power consumed by the CFJ actuators are absorbed by the inlet system as exergy increase. At the same time, the system exergy is further increased by 22% more than the CFJ energy consumption due to removal of flow separation that reduces entropy increase.

1. Introduction

Active flow control (AFC) has attracted broad interest recently to improve flow quality such as separation elimination by adding external energy to the flow. Since it consumes energy, an AFC is thus desired to have high effectiveness, which may include flow separation elimination, lift enhancement, drag reduction, *etc*. An equally important measure of merit is that the AFC should have low energy expenditure to benefit the system energy efficiency as a whole. However, AFC research community in general has mostly focused on the effectiveness, not enough on the AFC energy expenditure and its impact on the system energy benefit. The reason may be because the AFC energy expenditure depends on the AFC flow path, the flow sources, and sinks. For some non-zero-net-mass-flux AFC methods such as injection only or suction only, the AFC system is not a closed self-contained system, and the flow path and the sources/sinks are unknown. The energy expenditure hence could be difficult to estimate.

One way to measure AFC energy efficiency is to examine whether the available amount of work or energy state of the whole system, namely Exergy, can be increased more than the consumed energy by the AFC. A desirable AFC is to have high effectiveness and low energy expenditure so that the system exergy can be leveraged by the improved flow quality. However, little research is done so far to evaluate the exergy of AFC and its impact on the system. Based on the previous work [1], this paper is to address this issue by applying co-flow jet (CFJ) active flow control to an aircraft serpentine duct inlet that is massively separated.

Serpentine ducts (S-ducts) are widely used in modern aircraft. Combined with boundary layer ingestion, a short S-duct is able to significantly reduce fuel consumption and ram drag [2,3]. For military aircraft, S-ducts reduce radar cross-sectional visibility due to the buried engines [4,5]. However, a major challenge of S-ducts is the flow distortion caused by flow separation, which is often induced by the high wall curvature at the duct bend. The consequences of inlet distortion can be serious, such as reducing compressor stall margin and efficiency, exciting fan blade high cycle fatigue vibration, decreasing aircraft maneuverability, and reducing the engine life span.

To mitigate the flow separation inside S-ducts, passive flow control methods using vortex generators (VG) are studied numerically and experimentally [6–9]. For the CFD simulated vortex generators (VG), the engine face distortion and flow unsteadiness of the

* Corresponding author.
E-mail addresses: kxx50@miami.edu (K. Xu), gzha@miami.edu (G. Zha).

https://doi.org/10.1016/j.ast.2022.107746

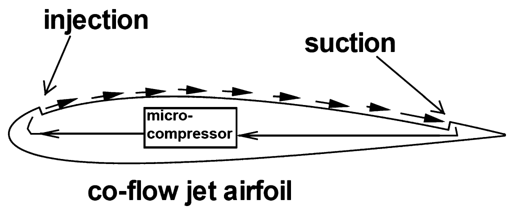

Fig. 1. Sketch of a CFJ airfoil.

M2129 S-duct could be reduced by 80% [10]. Jirasek *et al*. [11] conduct an optimization study of vortex generators and find the effectiveness mainly depends on the VG height and location in the flow separation zone. Yi *et al*. [12] optimize the vortex generators using the discrete adjoint approach, which is able to reduce the DC_{60} up to 97%.

Active flow control (AFC) has a high potential to improve flow performance by adding energy to the flow and has attracted a lot of interest for S-duct distortion mitigation. The fluidic-oscillating jets active flow control [13,14] are used on an offset diffuser to generate streamwise vorticity and reduce total pressure distortion. It is able to reduce the Aerodynamic Interface Plane (AIP) distortion by more than 60%. To reduce the required engine bleed mass flow, Harrison *et al*. [15] conducted a numerical and experimental study to augment blowing flow with the flow entrained from the suction holes using an ejector-pump concept. It is able to reduce the engine-face distortion by 75%. This method is not a zero-net-mass-flux flow control and requires engine bleed that would affect the engine system efficiency. Rudin *et al*. [16] numerically apply steady suction upstream and steady/oscillatory blowing downstream in the diffusion region and achieve an improvement of 4.3% in total pressure recovery and 70% in DC_{60} reduction. Even though this method may potentially achieve zero-net-mass-flux flow control, the energy expenditure may be high because it sucks the flow upstream where the pressure is low and blows the flow downstream where the pressure is high. Nonetheless, both the works in Ref. [15,16] do not study the energy expenditure of their AFC and the impact on the inlet-engine system.

The Co-flow Jet (CFJ) active flow control [17–29] is demonstrated to have high effectiveness and efficiency, where the effectiveness means a high performance improved by the flow control, such as lift enhancement, drag reduction, separation removal; the efficiency indicates a low energy expenditure of the flow control. As sketched in Fig. 1, a CFJ airfoil draws a small amount of mass flow into the airfoil near the trailing edge, pressurizes, and energizes it using a micro-compressor system embedded inside the airfoil, and then tangentially injects the same mass flow near the leading edge in the main flow direction.

Recently, Xu *et al*. [29–31] investigate the separation mechanism and energy expenditure of the CFJ. They observe that the CFJ is most effective and efficient to be applied in adverse pressure gradients. It is desirable to have a sufficiently long distance between the injection and suction slot so that the CFJ and the main flow can have thorough mixing to minimize the energy expenditure. Xu and Zha [1,32] apply CFJ to the M2129 S-duct and effectively mitigates the flow separation and distortion with various throat Mach numbers. The low energy expenditure of the co-flow jet is attributed to two factors: 1) injection at upstream where the main flow pressure is low and suction at downstream where the main flow pressure is high; 2) Zero-net-mass-flux flow control. These unique features distinguish CFJ from all other AFC such as those used in Ref. [15,16].

The purpose of this paper is two-fold: 1) apply co-flow jet flow control for the first time to an S-duct to demonstrate its high effectiveness, which includes eliminating the flow separation and distortion, and improving total pressure recovery; 2) assess the CFJ AFC's energy expenditure and its impact on the inlet-engine system via exergy analysis. To the authors' knowledge, this is the first effort to analyze the energy benefit of active flow control for a thermal fluid engine system. The adopted exergy analysis methodology is not limited to the CFJ S-duct engine system. It is also applicable to general thermal fluid systems with AFC.

2. Parameters for co-flow jet S-duct

To facilitate the description of CFJ S-duct performance, a few important parameters are given below.

2.1. Jet momentum coefficient (C_μ)

The injection jet momentum coefficient C_μ is used to describe the CFJ strength as:

$$C_\mu = \frac{\dot{m}_j U_j}{0.5\rho_i {U_i}^2 A_i} \tag{1}$$

where $\dot{m}_j$ is the CFJ mass flow, U_j is the mass-averaged CFJ injection velocity, ρ_i and U_i denote the S-duct inlet density and velocity, and A_i is the inlet area of the S-duct.

2.2. Power coefficient (P_c)

The CFJ power required is determined by the CFJ total enthalpy rise from the suction duct outlet to the injection duct inlet [18]. The total enthalpy rise can be achieved by the embedded micro-compressors. The power required by the CFJ can be expressed as:

$$P_{CFJ} = \dot{m}_j H_{j2}(\Gamma_j^{\frac{\gamma-1}{\gamma}} - 1) \tag{2}$$

where H_{j2} is the CFJ total enthalpy at the suction slot, Γ_j is the total pressure ratio between the injection and suction. The actual power consumed also depends on the pumping system efficiency, η_{CFJ}, as:

$$P_{act} = \frac{P_{CFJ}}{\eta_{CFJ}} \tag{3}$$

The power required defined by Eq. (2) is an important measure of merit of active flow control. The pumping efficiency depends on the fluidic actuator design and manufacturing. For aerospace applications, the micro-compressor actuators with diameters of 5 cm and above can achieve high efficiency of over 80% [27,33–35]. To focus on the fluid mechanics of CFJ AFC, the present work only studies the power required defined by Eq. (2).

Eq. (2) indicates that the power required by CFJ is linearly determined by the mass flow rate and exponentially determined by the total pressure ratio. This relationship in fact applies to all the active flow controls that are based on fluidic actuators. Thus, C_μ can not be used to represent the power consumption of active flow control [18,29]. For example, a high C_μ could have a substantially lower power consumption than a smaller C_μ if the large C_μ is created by a high mass flow rate and low jet velocity, which requires a significantly lower total pressure ratio [29,36,37]. The power coefficient is defined as:

$$P_c = \frac{P_{CFJ}}{0.5\rho_i U_i^3 A_i} \tag{4}$$

where P_{CFJ} is the CFJ required power defined in Eq. (2).

2.3. Total pressure recovery (δ)

The total pressure recovery (δ) is used to evaluate the efficiency of an S-duct. The higher the δ, the higher the efficiency and lower the loss. As expressed by Eq. (5), it is the total pressure ratio between the aerodynamic interface plane (AIP) outlet and the S-duct inlet, where AIP refers to the engine face of the S-duct.

$$\delta = \frac{Pt_{AIP}}{Pt_i} \tag{5}$$

2.4. Distortion coefficient (DC_{60})

The distortion coefficient DC_{60} [38,39] is used to quantify the severeness of distortion at the S-duct AIP. It is computed based on the most distorted sector of 60°. The formulation of DC_{60} is the following,

$$DC_{60} = \frac{Pt_{AIP} - Pt_d}{q_{AIP}} \tag{6}$$

where Pt_{AIP} is the averaged total pressure at AIP, Pt_d is the averaged total pressure in the worst 60 degree sector of AIP, and q_{AIP} is the averaged dynamic pressure at AIP. Since Pt_d is in the severe distortion area with more loss, the value is expected to be lower than Pt_{AIP}. The values used in the present paper for DC_{60} calculation follow the same data reduction routine used in the experiment [40,41], where Pt_{AIP} and Pt_d are calculated based on the 72 probes for total pressure measurement with the locations described in the experiment.

2.5. Compressor isentropic efficiency (η) and actual work (W)

To facilitate the exergy analysis of the engine system, the isentropic efficiency of the engine compressor downstream of the S-duct is given below:

$$\eta = \frac{W_s}{W} = \frac{\dot{m} H_{01}[(\frac{p_3{}^*}{p_1{}^*})^{\frac{\gamma-1}{\gamma}} - 1]}{W} \tag{7}$$

where $\dot{m}$ is the compressor mass flow, H_{01} is the total enthalpy at the AIP, W_s and W are the compressor isentropic work and actual work respectively to increase the total pressure from $p_1{}^*$ at the AIP as the compressor entrance to $p_3{}^*$ at the compressor outlet.

The actual work required by the compressor then can be expressed by:

$$W = \frac{\dot{m} H_{01}[(\frac{p_3{}^*}{p_1{}^*})^{\frac{\gamma-1}{\gamma}} - 1]}{\eta} \tag{8}$$

3. The numerical algorithm

The in-house high order accuracy CFD code Flow-Acoustics-Structure Interaction Package (FASIP) is used to conduct the numerical simulation. The 3D Reynolds Averaged Navier-Stokes (RANS) equations with one-equation Spalart-Allmaras [42] turbulence model is used. A 3rd order WENO scheme for the inviscid flux [43–45] and a 2nd order central differencing for the viscous terms are employed to discretize the Navier-Stokes equations. The low diffusion E-CUSP scheme used as the approximate Riemann solver suggested by Zha *et al*. [46] based on the Zha-Bilgen flux-vector-splitting scheme [47] is utilized with the WENO scheme to evaluate the inviscid fluxes. Implicit time marching method using Gauss-Seidel line relaxation is used to achieve a fast convergence rate [48]. Parallel computing is implemented to save wall clock simulation time [49]. The FASIP code is intensively validated for various CFJ flow control simulations including airfoils [18–21,25,26,50], E-plane [24], control surface [28], and NASA hump [29–31].

4. Results and discussions

4.1. Baseline serpentine duct

4.1.1. Baseline geometry

The AGARD baseline serpentine duct (S-duct) tested and studied in [40,51] shown in Fig. 2 is used in the present study. The throat is located at the origin point of the axial axis. The S-duct is 2.001 ft in length and the throat is 0.4225 ft in diameter, which is located at the end of the inlet constant-area section. The outlet diameter is 0.5 ft with a diverging area ratio of outlet to throat of 1.4. The engine face, or the aerodynamic interface plane, is located 1.6 ft downstream of the duct throat. In the experiment, a center body (not shown) is located at the outlet and extended upstream to the AIP, occupying a cross-sectional area of 7% of AIP. The center-body is not simulated in the present study, similar to the practice adopted by other researchers [10–12] because its influence on the upstream flow distortion of the S-duct is observed to be minimal. The duct inlet boundary conditions for the simulation are adopted from the AGARD test cases, which have a total pressure of 101,216 Pa, total temperature of 293 K, and Reynolds number (Re) of 1.85 million (based on throat diameter). The inlet velocity is imposed to be normal to the inlet surface.

4.1.2. Numerical validations

The 3D mesh topology is shown in Fig. 3. The plots on the left bottom of Fig. 3 are the 2-D mesh slides at the symmetry plane, which show that the grids of CFJ injection and suction ducts are one-to-one connected with the main-duct mesh. Only half of the S-duct is simulated due to the symmetric geometry and steady-state flow. The S-duct bend section has a more refined mesh. A butterfly grid topology is used for the duct cross-section as shown in Fig. 3 (right). The overall mesh size is 2.0 million points with 105 × 281 × 68 points in the streamwise, circumferential and radial directions respectively. The outlet boundary condition uses a specified static pressure that matches the experimental throat Mach number. The no-slip wall boundary condition is enforced on all the duct walls. A symmetry boundary condition is applied on the S-duct symmetric plane.

The plot on the left of Fig. 4 shows the Mach number contours of the baseline S-duct at the symmetric plane with the throat Mach number (M_{th}) of 0.79. The plot on the right of Fig. 4 shows the distribution of total pressure recovery at AIP. Massive flow separation occurs at the duct bend section, which causes significant total pressure loss and distortion at the bottom of AIP. The predicted total pressure recovery (δ) is 95.9%, which is in excellent agreement with the experimental value of 95.7%. The predicted distortion coefficient DC_{60} at AIP is 41.7%, which is also in good agreement with the experiment and has a deviation from the measured value of 40.4% by about 3.2%.

Fig. 5 shows the wall static pressure distribution along the axial direction, where θ of 0° and 180° are the circumferential angles representing the top wall surface and the bottom wall surface of the duct on the symmetric plane.

The mesh refinement results are also presented in Fig. 5, where S×2, W×2, and C×2 stand for the doubled mesh sizes in streamwise, radial, and circumferential directions respectively. A very good agreement is achieved between the predicted results and the experiment. The deviation from the experiment is slightly more on the bottom surface, which has the flow separation due to the S-duct bend. The mesh refinement studies generate little difference for the pressure distribution as shown in Fig. 5. The total pressure

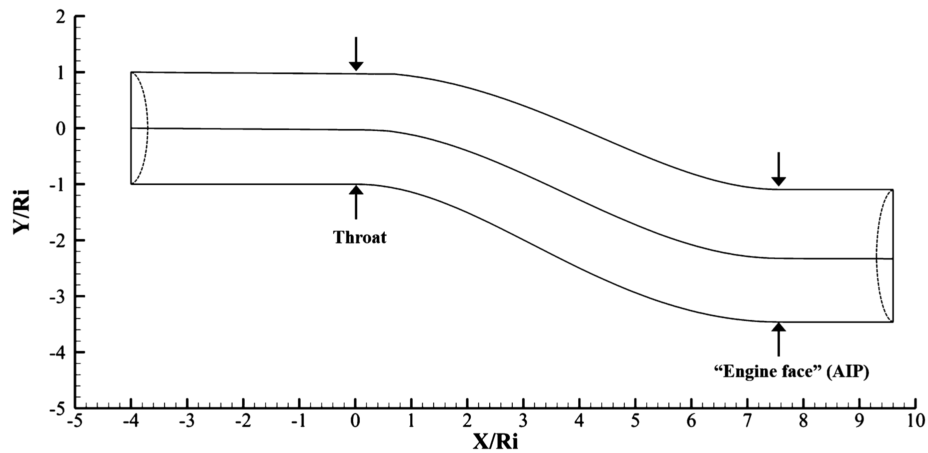

Fig. 2. Side-view of the baseline S-duct.

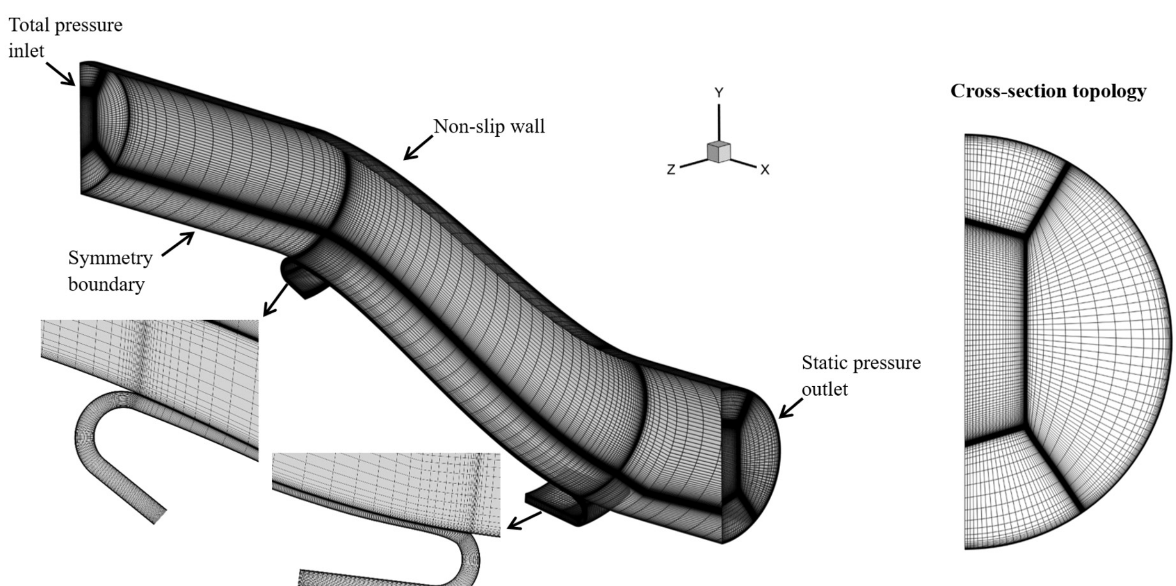

Fig. 3. Mesh topology of the CFJ S-duct.

Table 1
Simulation results of the baseline S-ducts with mesh refinement studies.

Cases	Mesh size	Re	δ (%)	DC_{60} (%)
EXP	-	-	95.7	40.4
Baseline mesh	105 × 281 × 68	1.85×10^6	95.9	41.7
Streamwise × 2	210 × 281 × 68	1.85×10^6	95.8	40.8
Circumferential × 2	105 × 562 × 68	1.85×10^6	95.6	42.5
Radial × 2	105 × 281 × 136	1.85×10^6	95.7	40.6

recoveries of the refined meshes shown in Table 1 all have a less than 0.2% deviation from the experiment. These results show that the present simulation with the baseline mesh size is converged based on the mesh size. The predicted distortion of the mesh refinement study has a maximum 5% deviation from the experiment, which is acceptable as distortion is more sensitive to local separated flow structure that is difficult for a RANS model to predict accurately.

4.2. Co-flow jet serpentine duct

4.2.1. Geometry of the CFJ S-duct and BCs

A co-flow jet S-duct configuration is shown in Fig. 6 to illustrate how CFJ is implemented with the S-duct. The CFJ is created by placing an injection duct (in blue) at the start of the duct turning immediately downstream of the throat and a suction duct (in orange) downstream of the S-duct bend. The micro-compressor is not simulated but is numerically treated by applying the exact compressor boundary conditions, which have the total pressure, total temperature, and flow angle specified at the injection duct inlet. At the compressor inlet (suction slot outlet), static pressure is iterated to match the compressor outlet mass flow. A specified C_μ is achieved by iterating the injection total pressure. The same mass flow rate of injection and suction is achieved via iterations of the suction outlet static pressure. The injection jet enters the duct tangentially to the local wall surface. This CFJ compressor BC has been extensively validated in CFJ airfoils [18–21,27], CFJ control surfaces [28], and CFJ micro-compressor with ducts [33–35].

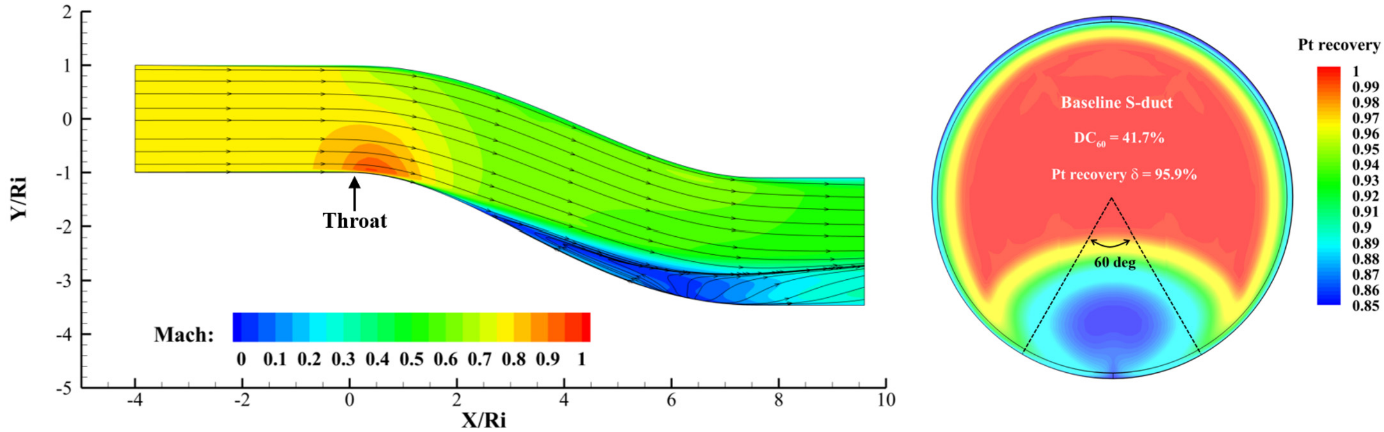

Fig. 4. Mach contour of the baseline S-duct and total pressure recovery at AIP.

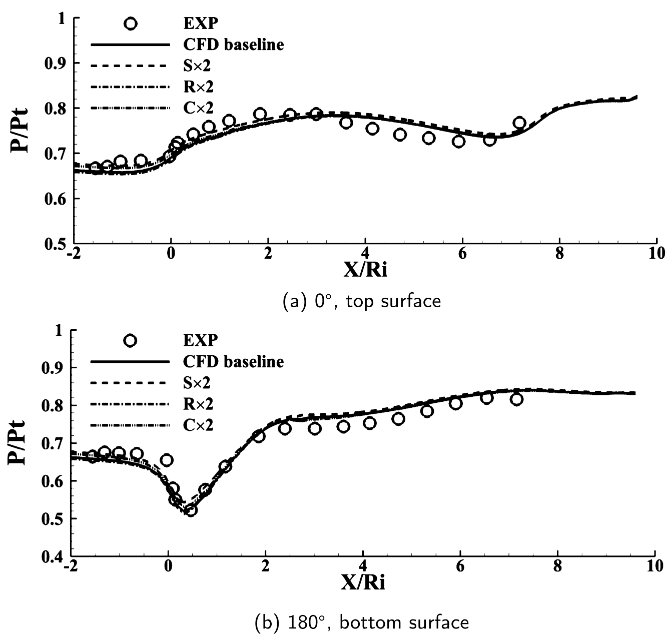

(a) 0°, top surface

(b) 180°, bottom surface

Fig. 5. Wall static pressure distributions.

Compared with the actuator disk boundary condition to mimic the compressor pressure rise, the advantages of the BC used in this paper are: 1) It accurately simulates the compressor inlet and outlet conditions; 2) It does not impose the actuator disk parameter jump condition, which is often treated as a discontinuity and may cause numerical instability, in particular when the pressure rise is large. The disadvantage of this BC is that it is more time-consuming because it involves two layers of iteration when C_μ is specified.

To make the injection and suction slots smoothly merged with the S-duct wall, the bottom wall surface is translated slightly outward by a concentric circle with the radius increased by 0.5%R_i. A circumferential-bull-horn-shaped geometry (shown in Fig. 6 (b) left) is adopted for the CFJ injection and suction slots to minimize the separation caused by the CFJ duct wall on both sides. The circumferential width of the CFJ slot is measured by its circumferential angle (β) as shown in Fig. 6.

Various trade studies of different injection locations, suction locations, and sizes are conducted. Three representative configurations of the CFJ S-ducts with two circumferential angles (β) of suction slots and two suction locations are presented herein. The injection location is fixed at 0.47 X/R_i where the adverse pressure gradient begins as shown in Fig. 4 and 5. CFJ is more effective and efficient to be used in adverse pressure gradient (APG) [29–31]. The CFJ's high effectiveness in APG is due to the enhanced turbulent diffusion [29]. The high efficiency is because the lower entropy generation in APG reduces the loss and power required by the micro-compressor [30,31]. More details of the geometrical parameters are given in Table 2.

Table 2
Geometrical parameters of CFJ S-ducts, locations (Loc) and circumferential width (β).

Cases	Inj Loc (X/R_i)	Suc Loc (X/R_i)	Inj β (°)	Suc β (°)
1	0.47	6.63	100	90
2	0.47	3.29	100	90
3	0.47	3.29	100	120

The relative positions of the injection and suction slots with their circumferential widths are demonstrated in Fig. 7. Case 1 and 2 have different axial suction locations, but have the same circumferential width β angle of the injection slot of 100°. The suction slots β angles of Case 1 and 2 are 90° and are also located at different streamwise locations. Due to the different streamwise locations and diameters, the circumferential widths covered by the injection and suction slots are roughly the same as shown in Fig. 7 on the left and in the middle. Case 1 has the suction located more downstream at X/R_i=6.63 than that of Case 2 at X/R_i=3.29. This makes the suction slots of Case 1 and Case 2 located at different transverse positions. Even though Case 2 has the same circumferential angle of 90° as Case 1, the circumferential width of the Case 2 suction slot is actually slightly smaller than that of Case 1 due to the smaller diameter. The comparison of Case 1 and 2 is primarily to show the streamwise location effect of the suction slot. Case 3 has the same suction axial location as Case 2, but the circumferential width angle β is increased by 30° to show the effect of the suction slot width. The momentum coefficient (C_μ) of 0.46 is used for both Cases 2 and 3. Case 1 has a slightly higher C_μ of 0.49 to reach the same power coefficient (P_c) as Case 2. This is to achieve the comparison of control effectiveness with the same energy consumption.

4.2.2. Flow control results and discussions

Fig. 8 shows the Mach number contours and streamlines at the symmetric plane for the three CFJ S-ducts. Compared with the baseline S-duct separated flow shown in Fig. 4 (left), all these three CFJ cases have the flow separation removed. The high-energy jet through the injection slot energizes the main flow boundary layer to overcome the adverse pressure gradient at the S-duct bend.

Comparing the injection and suction axial location in Table 2 with the pressure distribution on the bottom wall in Fig. 5 (b), it is shown that the injection slot of all the three CFJ S-ducts is located

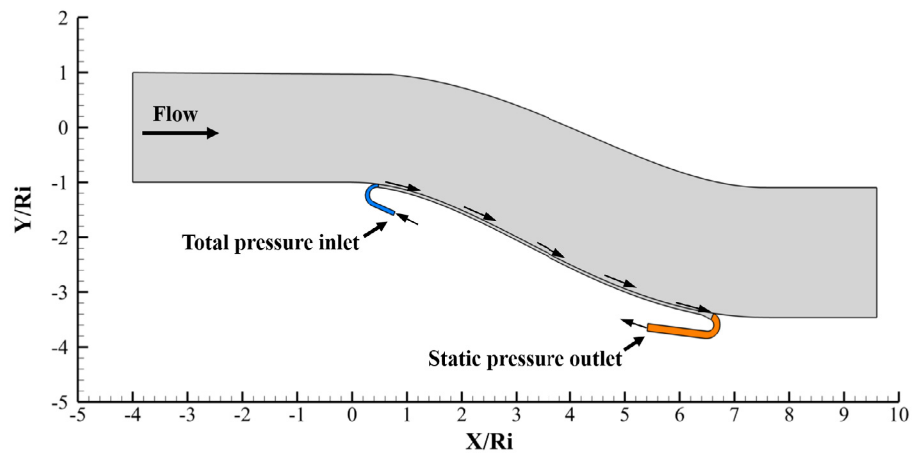

(a) CFJ S-duct at symmetric plane view

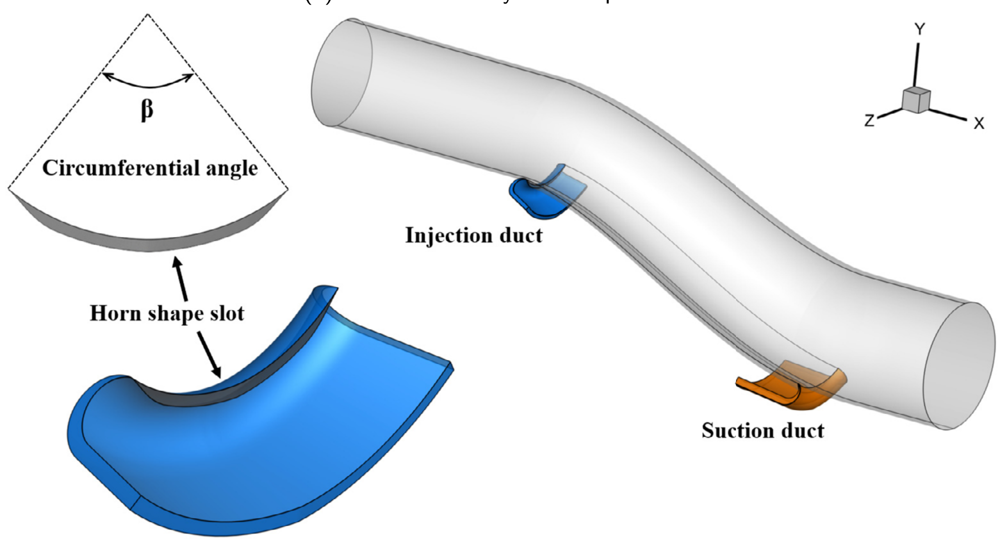

(b) 3D geometry of CFJ S-duct

Fig. 6. CFJ S-duct configuration. (For interpretation of the colors in the figure(s), the reader is referred to the web version of this article.)

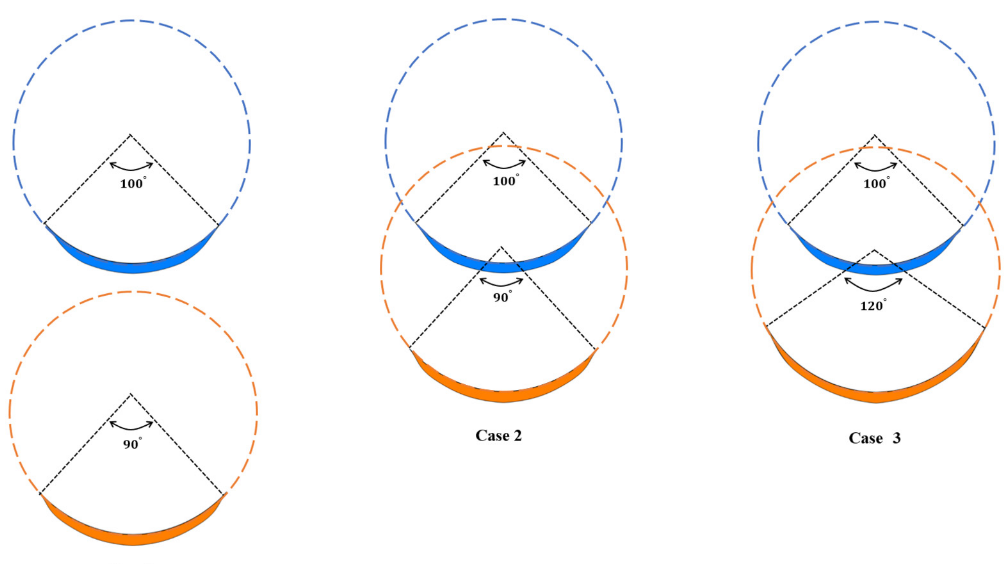

Fig. 7. Locations and sizes of the CFJ injection and suction slots.

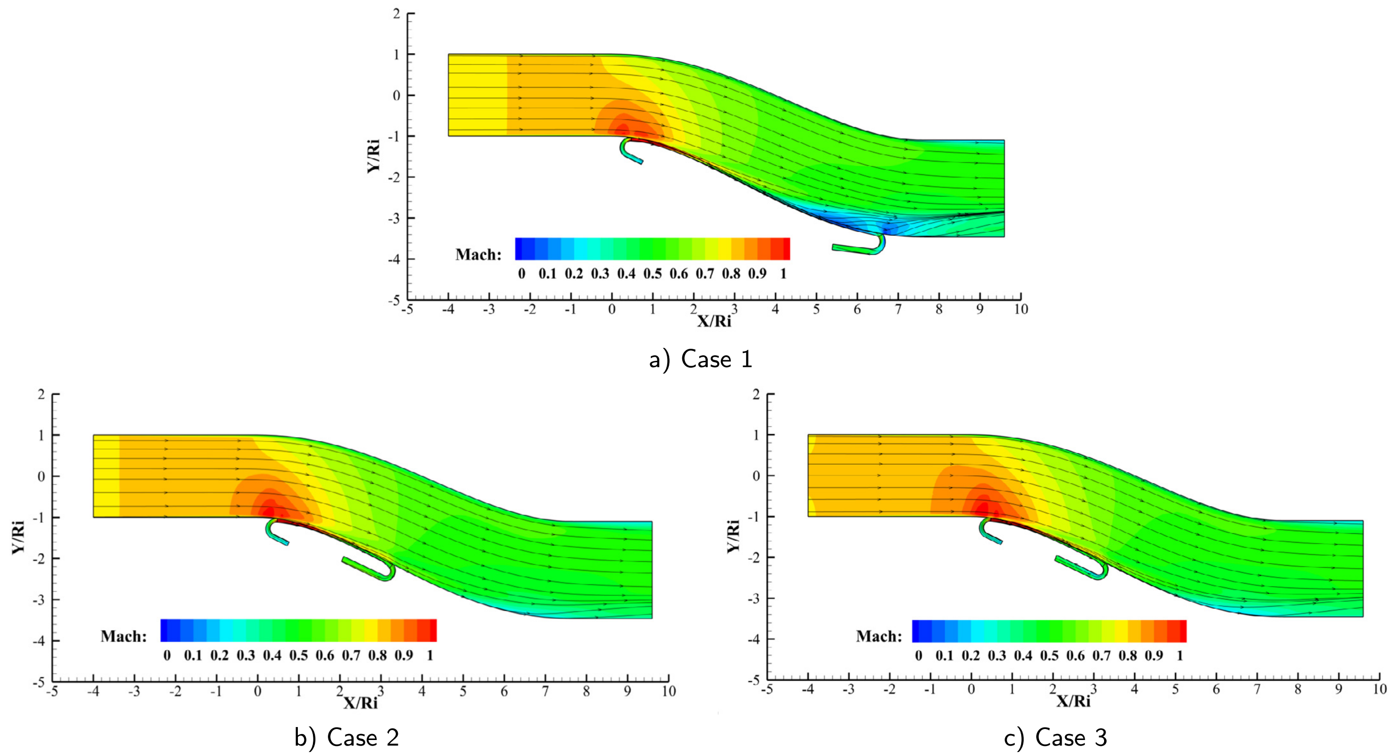

Fig. 8. Mach contours of the CFJ S-ducts at symmetry plane.

at the lowest pressure position X/R_i =0.47. The adverse pressure gradient (APG) rapidly increases from this point to X/R_i=2 and becomes mild downstream. The CFJ S-duct Case 1 has the suction located downstream at X/R_i=6.63 in the deep separation region as shown in Fig. 4. Whereas, the CFJ S-duct Case 2 and 3 have the suction located significantly more upstream at X/R_i=3.29 where the separation starts. The pressure rise between the injection location and suction location of CFJ S-duct Case 2 and 3 is large, but is mild between the suction locations of CFJ Case 1 and 2. In other words, the pressure difference between CFJ S-duct 1 and 2 is not large, but the flow separation severeness is very large.

Fig. 8 indicates a low Mach number zone at the duct bend in Case 1 with the suction location at 6.63 X/R_i, but the flow is not separated. The suction location 3.29 X/R_i for Cases 2 and 3 is slightly downstream of the onset of flow separation as shown in Fig. 4, which is the location that most effectively energizes the flow boundary layer [29–31]. Case 1 placing the suction at 6.63 X/R_i in the fully separated region is not efficient and requires higher energy consumption to barely remove the flow separation. The comparison in Fig. 8 indicates that the coupling effect of the injection and suction is important.

Fig. 9 compares the normalized total pressure contours at four same streamwise locations for the baseline S-duct and CFJ S-duct Case 1, 2, and 3. A high-energy flow with high total pressure is injected into the flow by CFJ as highlighted by the red rectangle. As flow approaches downstream, the high-energy jet mixes with the retarded flow at the duct bend and energizes the boundary layer. Different behaviors of the jet mixing are observed for the three CFJ cases. The high-energy injection jet in Case 1 as shown in Fig. 9 (b) is significantly dissipated before approaching the suction slot. The boundary layers of the Cases 2 and 3 are further energized by their suction located more upstream and are able to enhance the energy transfer and remove the low momentum flow as shown in Fig. 9 (c) and (d).

The performance of CFJ cases (1-3) and the baseline S-duct at AIP is summarized in Table 3, where δ is the total pressure recovery and Γ_j is the required total pressure ratio of the CFJ micro-compressor actuator. $\Delta\delta$ is the improvement of total pressure recovery in percentage, and ΔDC_{60} measures the reduction of distortion coefficient in percentage. m_r is the ratio of the CFJ total mass flow rate to the mass flow rate of the S-duct.

Fig. 10 compares the AIP total pressure recovery (δ) contours of the CFJ S-ducts (right) and the baseline case (left). As shown in Table 3, the CFJ Case 1 duct substantially decreases the AIP distortion from 41.7% to 5.4% and increases the total pressure recovery from 95.9% to 97.6%. This is because the CFJ Case 1 removes the flow separation as shown in Fig. 8 and 9. Cases 2 and 3 are able to further drive down the distortion to 1.8% and 0.67% respectively. Case 3 essentially eliminates the flow distortion while increasing the total pressure recovery.

As shown in Table 3, the particularly encouraging result is that the optimal CFJ Case 3 is achieved solely by manipulating the CFJ configuration with the momentum coefficient C_μ and the CFJ power coefficient reduced compared with the CFJ Case 1. Comparing the results of CFJ Case 1 and 2 in Tables 3, CFJ Case 2 improves both the AIP distortion and total pressure recovery with the same CFJ power by moving the suction slot from the deep separation region to slightly downstream of the baseline separation onset location. Compared with CFJ Case 2, CFJ Case 3 further reduces the distortion and improves the total pressure recovery with even reduced CFJ power by increasing the suction slot circumferential angle. Table 3 also shows that the flow actuated by the CFJ Case 3 is 1.82% of the total inlet mass flow. Since CFJ is a ZNMF flow control, it has the advantage that the amount of the flow actuated by CFJ does not increase or decrease the mass flow of the inlet-engine system.

To understand the flow structures that bring the advantages of Case 3 over Case 2, Fig. 11 shows the wall static pressure contours and the near-wall streamlines of the two cases. The low energy zone observed in Fig. 10 (b) results from the low energy flow (marked as Flow 1) migrating from the side wall at the entrance to the bottom of the AIP as shown in Fig. 11 (a), which is

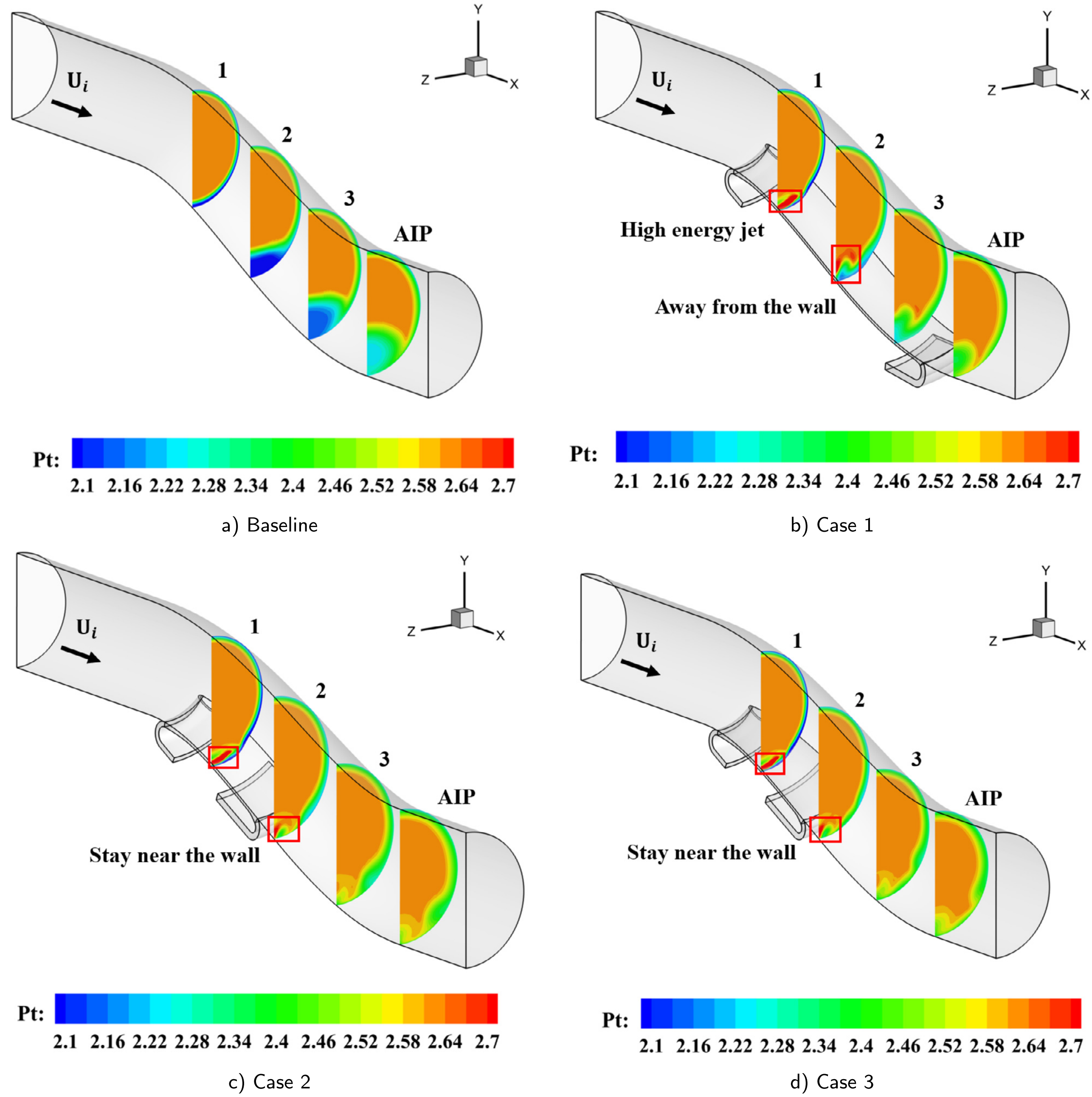

Fig. 9. Total pressure contours along stream-wise of the baseline and CFJ S-ducts.

Table 3
Performance of CFJ and baseline S-ducts at AIP.

Cases	C_μ	δ (%)	$\Delta\delta$ (%)	DC_{60} (%)	ΔDC_{60} (%)	Γ_j	P_c	m_r (%)
Baseline	-	95.9	-	41.7	-	-	-	-
CFJ-1	0.49	97.6	1.7	5.40	-87.1	1.61	0.23	1.94
CFJ-2	0.46	97.8	1.9	1.80	-95.7	1.63	0.23	1.82
CFJ-3	0.46	97.9	2.0	0.67	-98.4	1.60	0.22	1.82

driven by the swirl caused by the pressure and density gradient of S-duct. This phenomenon is also observed by Yi *et al*. [12]. As the CFJ suction slot (β) is increased from that of Case 2 to Case 3, the widened suction slot is able to withdraw most of the low energy flow migrating from the entrance as shown in Fig. 11 (b).

In terms of energy consumption, the CFJ power coefficient P_c required by Case 3 is the lowest, reduced by 4.5% compared with Case 1 and 2. Fig. 12 compares the contours of Mach number and entropy increase of Case 2 and Case 3 on the symmetric plane. The wider suction duct of Case 3 decreases the velocity inside as shown in Fig. 12 (a) and (b). The decreased velocity mitigates the viscous effects inside the suction duct and reduces the entropy increase near the duct wall especially at the duct turning section as shown in Fig. 12 (c) and (d). The lower total pressure loss of Case 3 reduces the power consumption of the CFJ micro-compressor. Overall, from both the aspects of control effectiveness and energy

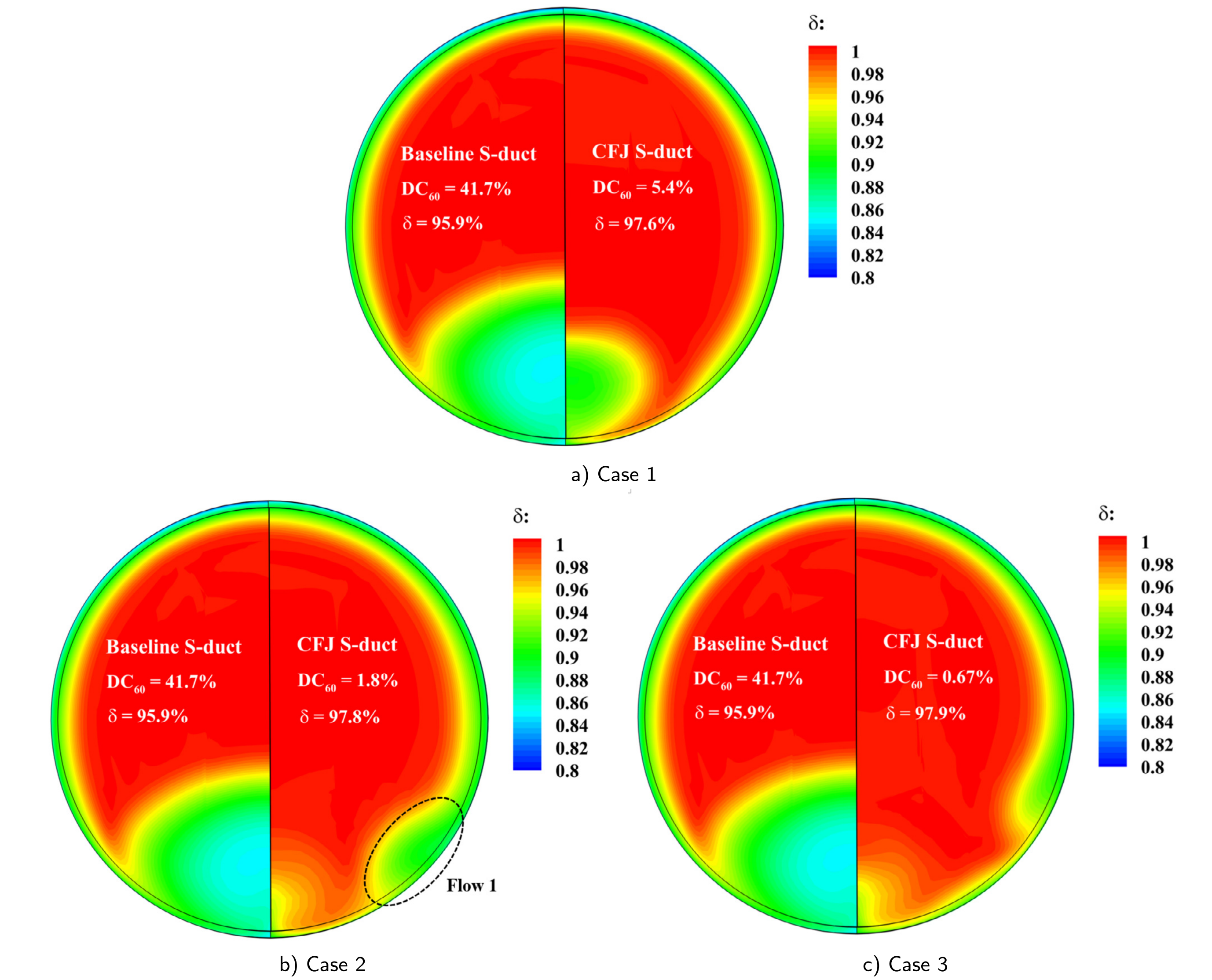

Fig. 10. Total pressure recovery distribution at AIP of CFJ S-ducts.

efficiency, Case 3 has the best performance among the three cases and is thus regarded as the optimum CFJ S-duct configuration in the present study.

4.3. Analysis of system exergy benefit

Based on the results achieved above, this section analyzes the exergy benefit of the co-flow jet active flow control for the S-duct inlet-engine system due to the flow separation elimination. From the aircraft system point of view, a high exergy inlet with more available work can reduce the energy consumption of the engine downstream.

Exergy (E_X) defined by Eq. (9) expresses the maximum available work of a thermal flow process [52], which is the S-duct herein.

$$
\begin{aligned}
E_X =& \dot{m}[(H_1 - H_i) - T_i(S_1 - S_i)] \\
=& \dot{m}(H_1 - H_i) + [-\dot{m}T_i(S_1 - S_i)] \\
=& E_{XH} + E_{XS}
\end{aligned}
\tag{9}
$$

where $\dot{m}$ is the mass flow rate of the S-duct, H is the mass-averaged total enthalpy, T is the mass-averaged static temperature, S is the mass-averaged entropy, $E_{XH} = \dot{m}(H_1 - H_i)$ is the exergy due to the system total enthalpy change, and $E_{XS} = -\dot{m}T_i(S_1 - S_i)$ is the exergy due to the entropy change. The subscripts i and 1 denote the location of the S-duct entrance and AIP respectively. Eq. (9) indicates that the system available work will increase if the total enthalpy of the system is increased. If the system has high entropy increase due to poor flow conditions such as flow separation, the system's available work will be decreased. The entropy change term $S_1 - S_i$ can be expressed by the thermodynamics relation:

$$
\Delta S = c_p ln(\frac{T_1{}^*}{T_i{}^*}) - Rln(\frac{p_1{}^*}{p_i{}^*}) \tag{10}
$$

where T^* is the mass-averaged total temperature and p^* is the mass-averaged total pressure. Substitute Eq. (10) to Eq. (9), we have

$$
\begin{aligned}
E_X =& \dot{m}[(H_1 - H_i) - T_i(c_p ln(\frac{T_1{}^*}{T_i{}^*}) - Rln(\frac{p_1{}^*}{p_i{}^*}))] \\
=& E_{XH} + E_{XS} \\
=& E_{XH} + E_{XT} + E_{Xp}
\end{aligned}
\tag{11}
$$

where $E_{XT} = -\dot{m}T_i c_p ln(\frac{T_1{}^*}{T_i{}^*})$, and $E_{Xp} = \dot{m}T_i Rln(\frac{p_1{}^*}{p_i{}^*})$

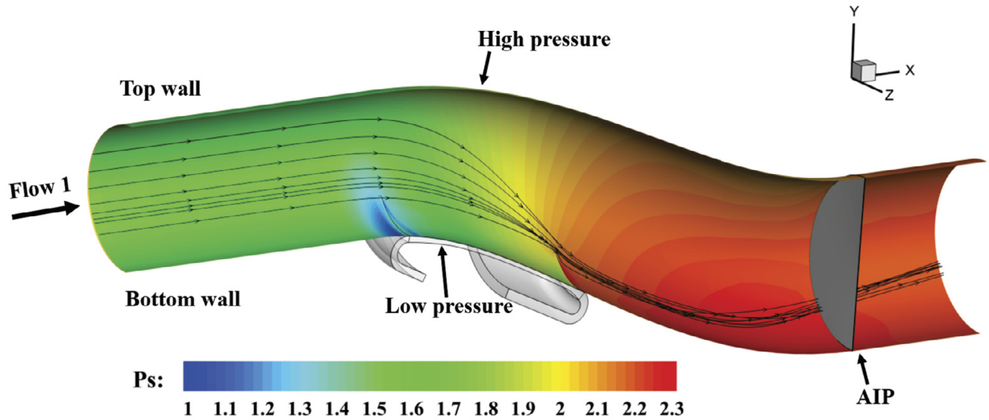

(a) Case 2

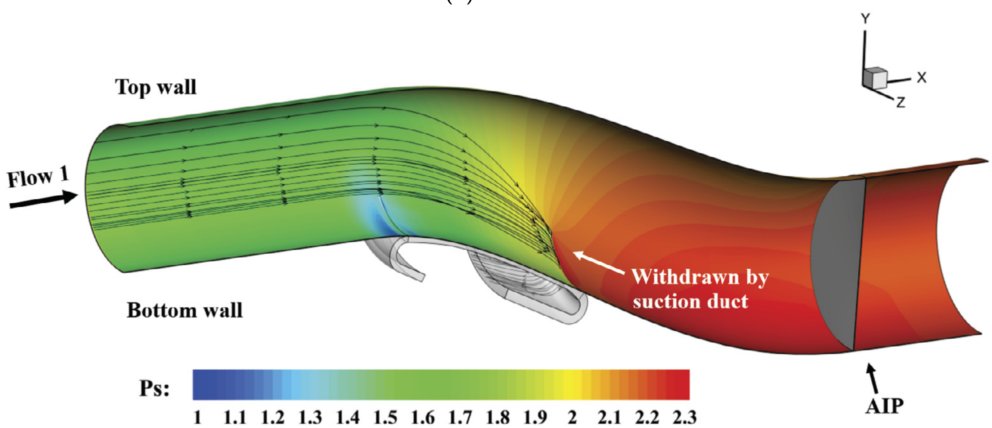

(b) Case 3

Fig. 11. Wall static pressure distribution of the CFJ S-ducts.

Eq. (11) indicates that the exergy is resulted from three sources: change of total enthalpy (E_{XH}), entropy variation due to total temperature increase (E_{XT}), and entropy variation due to total pressure loss (E_{Xp}). As shown in Eq. (9), exergy has the same unit as power.

Fig. 13 shows the control volume of the CFJ S-duct. The micro-compressor (MC) adds external work (e.g. electric power) to the control volume and increases the total enthalpy of the control volume.

Based on thermodynamics first law

$$dE = dQ - dW \tag{12}$$

where E is the energy of the system, Q denotes the quantity of heat supplied to the system, and W denotes the amount of thermodynamic work done by the system to its surroundings. For the control volume of Fig. 13 with the assumption of adiabatic flow, it receives external work from the micro-compressor, thus

$$dW = -P_{CFJ} \tag{13}$$

where P_{CFJ} is the micro-compressor power consumption defined by Eq. (2).

Since the CFJ is a ZNMF active flow control, the mass conservation of the control volume of Fig. 13 has

$$\dot{m}_i = \dot{m}_1 = \dot{m} \tag{14}$$

with the adiabatic process,

$$dE = -dW = \dot{m}(H_1 - H_i) = P_{CFJ} \tag{15}$$

The exergy Eq. (9) for CFJ S-duct then can be written as:

$$E_X{}^{CFJ} = P_{CFJ} + [-\dot{m}T_i(S_1 - S_i)] = P_{CFJ} + E_{XS}{}^{CFJ} \tag{16}$$

For the baseline S-duct with the adiabatic flow, $H_1 = H_i$, and $E_{XH} = 0$. Therefore,

$$E_X{}^{baseline} = E_{XS}{}^{baseline} \tag{17}$$

Eq. (16) indicates that the CFJ S-duct will absorb all the work provided by the micro-compressor to its exergy. If the flow condition is improved such as the removal of flow separation, the entropy increase will be reduced compared with that of the baseline S-duct. In that case, the system not only fully recovers the energy consumed by the CFJ and improves the flow condition, but also gains extra exergy due to the reduced entropy increase benefited from the improved flow conditions. The significance is that the total energy cost of the AFC will be fully translated to benefit the downstream engine system with extra energy gain except for the loss due to the irreversibility of the thermal flow process.

Fig. 14 shows the total temperature contours at various streamwise locations. The total temperature of the baseline S-duct remains constant throughout the duct, but the total temperature of the CFJ S-duct is increased in the area of CFJ applied due to the work transferred from the CFJ micro-compressor via flow mixing. Even though the CFJ reduces the S-duct total pressure distortion significantly, the added energy appears to create a total temperature distortion in a small region of the AIP. The effect of such total temperature distortion on the downstream engine is not expected to be significant but needs to be studied in the future.

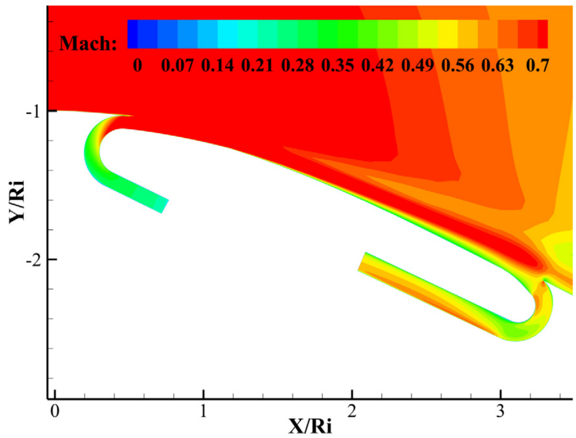

(a) Case 2, Mach number

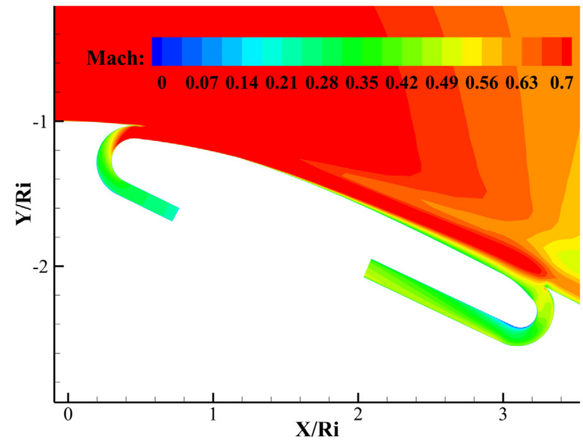

(b) Case 3, Mach number

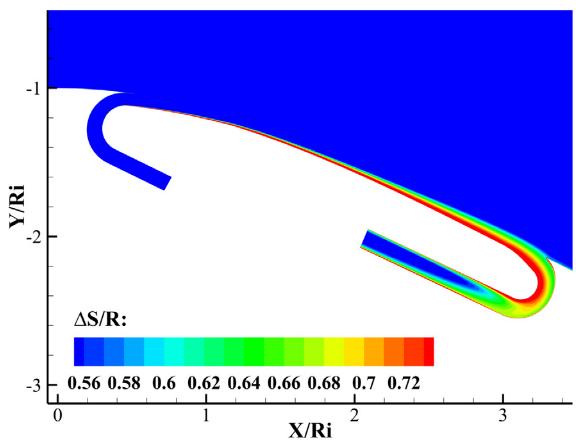

(c) Case 2, Entropy change

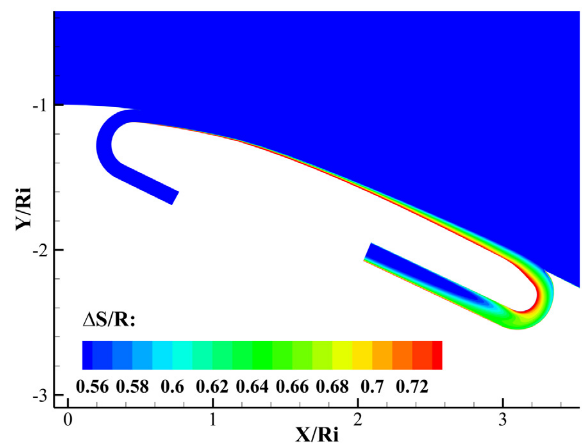

(d) Case 3, Entropy change

Fig. 12. Mach number and normalized entropy contours at symmetric view of the suction duct in Case 2 and Case 3.

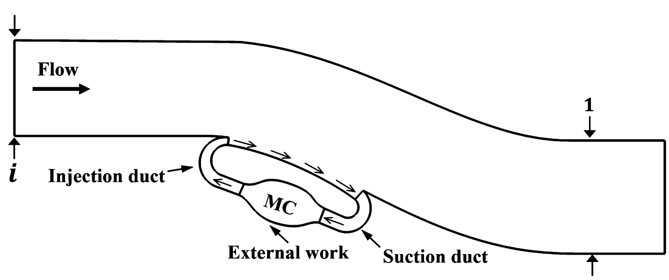

Fig. 13. Sketch of the work transfer between the CFJ micro-compressor (MC) and S-duct.

Eq. (18) uses an overline to denote the normalized exergy by the free-stream velocity, density, and reference area in the same way as the power coefficient (P_c) in Eq. (4).

$$\overline{E_X} = \frac{E_X}{0.5\rho_i U_i^3 A_i} \tag{18}$$

Using the same way, we can normalize $\overline{E_{XS}}$, $\overline{E_{XH}}$, $\overline{E_{XT}}$ and $\overline{E_{Xp}}$.

The energy benefit of the S-duct with CFJ is the exergy difference between the CFJ and baseline S-duct as expressed below based on Eq. (16) and (17),

$$\Delta E_X = {E_X}^{CFJ} - {E_X}^{baseline} =$$
$$P_{CFJ} + \Delta E_{XS} = P_{CFJ} + \Delta E_{XT} + \Delta E_{Xp} \tag{19}$$

Following Eq. (18), we also have the normalized $\overline{\Delta E_{XH}}$, $\overline{\Delta E_{XS}}$, $\overline{\Delta E_X}$, $\overline{\Delta E_{XT}}$, $\overline{\Delta E_{Xp}}$, $\overline{{E_X}^{CFJ}}$ and $\overline{{E_X}^{baseline}}$.

ΔE_X stands for the gain of the system available amount of work or gain of the exergy, which is obviously at the expense of the CFJ flow control energy consumption. The question of interest is whether such an exergy gain is greater than the cost of the CFJ energy consumption. The ratio of exergy increase to the power required ($EIPR$) of AFC defined below based on Eq. (19) can be used to measure the gain:

$$\begin{aligned} EIPR =& \frac{\Delta E_X}{P_{CFJ}} = 1 + \frac{\Delta E_{XS}}{P_{CFJ}} \\ =& 1 + \frac{\overline{\Delta E_{XS}}}{P_c} = \frac{\overline{\Delta E_X}}{P_c} \end{aligned} \tag{20}$$

If $EIPR > 1$, it means the system exergy is increased more than the AFC energy consumption attributed to the improved flow condition that reduces the entropy increase. If $EIPR = 1$, it meas the system exergy gain breaks even with the AFC energy consumption with no flow quality improvement. If $EIPR < 1$, it means the system exergy has a loss due to the AFC energy consumption with the flow condition deteriorated.

The general motivation of AFC is to improve the flow condition of a flow system with exergy gain. A desirable AFC for durable mission usage should have the following features: 1) low E_{XH}, meaning a low external energy source is required. For the CFJ S-duct case, it is a low CFJ power P_{CFJ}; 2) high $EIPR$ with a

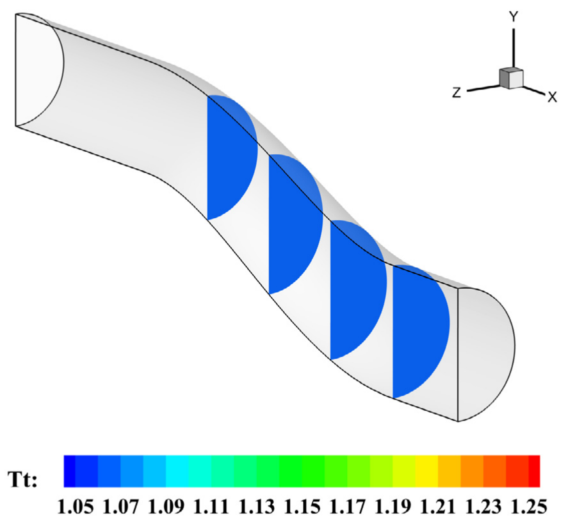

a) Baseline

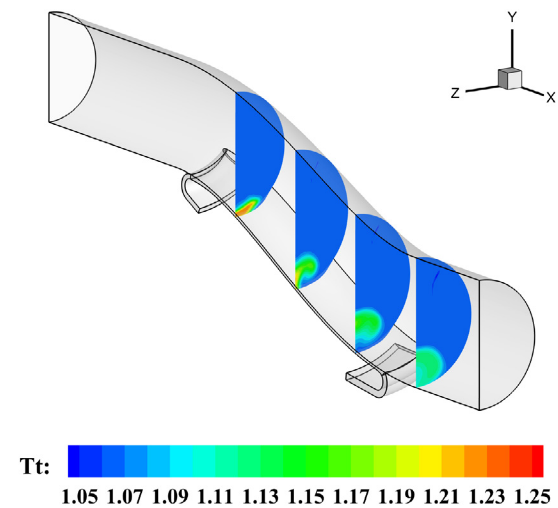

b) Case 1

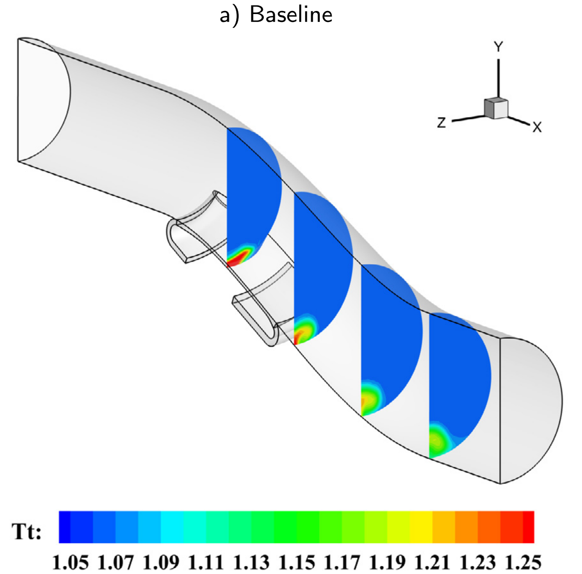

c) Case 2

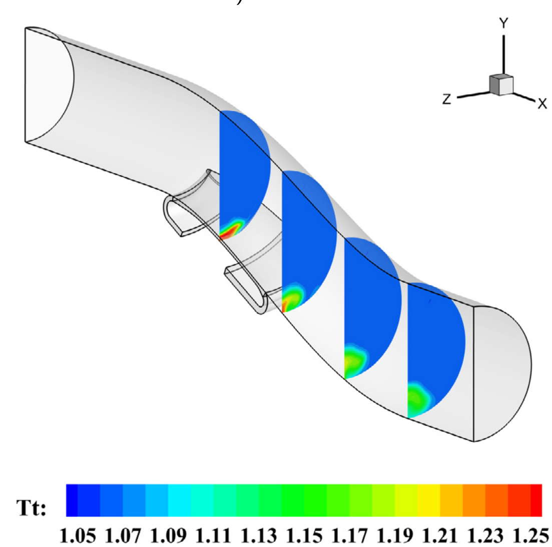

d) Case 3

Fig. 14. Total temperature contours along stream-wise of the baseline and CFJ S-ducts.

value greater than 1, meaning that the system gains exergy benefited from the flow conditions improved by the AFC, the larger the $EIPR$, the more energy-efficient is the AFC. As shown by Eq. (20), both a high $\overline{\Delta E_{XS}}$ and low P_c contribute to a large $EIPR$, which indicates an efficient AFC and flow system as a whole.

Table 4 compares the exergy of the baseline S-duct and the three CFJ cases with their $EIPR$. The negative sign of all the $\overline{E_X}$ in Table 4 means that all the S-duct systems have no available energy to do work due to the entropy increase from flow energy loss. For the baseline S-duct, the negative exergy is determined by the entropy rise due to total pressure loss since the total temperature is constant for the adiabatic flow. However, all the three CFJ cases have net exergy gain with $EIPR$ greater than 1 from 1.05 to 1.22.

The net exergy gain comes from $\Delta\overline{E_{Xp}}$ due to smaller entropy rise with attached flow and higher total pressure recovery achieved by the CFJ. However, the mixing process with the rise of total temperature also enhance entropy generation, and therefore $\Delta\overline{E_{XT}}$ significantly decreases the exergy gain. Overall, the increase of $\Delta\overline{E_{Xp}}$ outperforms the reduction of $\Delta\overline{E_{XT}}$ and results in a net exergy increase with $EIPR > 1$.

To have a qualitative understanding of the CFJ S-duct benefit to the inlet-engine system, we assume that the downstream of the S-duct is a jet engine axial compressor, which will have an isentropic efficiency (η) as expressed in Eq. (7). Assuming that the required compressor outlet total pressure $p_3{}^*$ and the compressor efficiency (η) are the same for the baseline S-duct and the CFJ S-duct, the compressor actual work Eq. (8) indicates that the compressor downstream will require less work with the CFJ S-duct due to higher $p_1{}^*$ benefited from the higher total pressure recovery. Furthermore, because the total pressure distortion at AIP is basically eliminated, the compressor efficiency will be increased and the compressor work will be reduced more. The amount of the compressor work reduced is caused by the upstream CFJ S-duct exergy increase, which is attributed to the CFJ active flow control. The other important benefit of eliminating the flow separation and distortion is to mitigate the high cycle fatigue of the compressor or fan blades downstream and avoid stall of the fan/compressor.

Table 4
Exergy and power consumption of the baseline and CFJ S-ducts.

Cases	$\overline{E_X}$	$\overline{E_{XT}}$	$\Delta\overline{E_{XT}}$	$\overline{E_{Xp}}$	$\Delta\overline{E_{Xp}}$	$\overline{\Delta E_{XS}}$	P_c	$EIPR$
Baseline	-0.443	-0.003	-	-0.440	-	-	-	-
CFJ-1	-0.212	-0.191	-0.188	-0.240	0.200	0.012	0.226	1.05
CFJ-2	-0.196	-0.186	-0.183	-0.223	0.217	0.034	0.218	1.16
CFJ-3	-0.186	-0.183	-0.180	-0.213	0.227	0.047	0.213	1.22

4.4. Potential application considerations

In actual applications, the CFJ micro-compressor actuators may decrease the engine system weight compared with using engine bleed for the flow control. This is because the micro-compressors have higher power density (kw/kg) due to much higher RPM (e.g. 100k) than those of aircraft engine compressors and fans. The weight introduced by the micro-compressors will be less than increasing the engine size and power for the bleed. The system complexity is also expected to be reduced because the micro-compressors can be controlled locally without the long ducts transporting the engine bleed air.

CFJ is shown to be reliable and robust to have a broad range of working conditions such as variation of angle of attack [50], flight Mach number [32], *etc*. At different flight conditions, the CFJ can be controlled by varying its jet strength C_μ, which is controlled by the power (i.e. RPM) of the CFJ micro-compressor actuators. As an example with the throat Mach number varying from 0.42 to 0.79, our previous study [32] indicates that the CFJ S-duct can eliminate the flow separation in all conditions and maintain a low distortion coefficient of less than 1%.

The annular injection and suction slots will not be continuous circumferential open groove. This is because CFJ is usually generated by embedding a series of micro-compressors circumferentially [27]. Each micro-compressor has its own duct. The duct walls will be used as the supporting struts to enhance the structure strength and integrity. Overall, a S-duct inlet is to diffuse the flow and is not a highly loaded component, thus structure integrity would not be a serious challenge.

5. Conclusions

This validated numerical study demonstrates for the first time that the CFJ AFC is effective and energy efficient to improve the flow quality of a S-duct inlet and increase the efficiency of the inlet-engine system as a whole. It can not only eliminate the flow separation and distortion, but also leverage the exergy state of the inlet system with the available work increased more than the CFJ power consumption. Three cases of the CFJ configuration trade study with two suction locations and slot widths are presented. The optimum configuration of the CFJ S-duct virtually eliminates the distortion by reducing DC_{60} from 41.7% to 0.67%. At the same time, the total pressure recovery is increased by 2.0%.

To effectively use CFJ for a S-duct, the overall coflow jet should be immersed in the adverse pressure gradient region. Both the CFJ injection slot size and location affects the AFC control effectiveness and efficiency. Placing the suction slot at the separation onset location is more efficient than placing it in the deep separation region. A wider suction slot with a circumferential angle of 120° is more effective than a narrower one of 90° to remove the low momentum flow migrating from the inlet entrance side wall.

A parameter, $EIPR$, is introduced to measure the merit of an AFC by calculating the ratio of exergy increase to the power required by the AFC. The larger the $EIPR$, the more efficient of the AFC system. If $EIPR$ is greater than 1, the system recovers all the AFC energy consumption and also gains efficiency benefited from the improved flow quality such as removal of flow separation. Attributed to the zero-net-mass-flux control, all the power consumed by the CFJ actuators in this study are absorbed by the CFJ S-duct system as exergy increase. Benefited from the removed flow separation at the same time, the system exergy is further increased with $EIPR = 1.22$, which means the inlet-engine system does not only fully recover the CFJ energy expenditure, but also has a net exergy gain of 22% more than the CFJ energy consumption.

Declaration of competing interest

The authors declare the following financial interests/personal relationships which may be considered as potential competing interests: Gecheng Zha reports a relationship with CoFlow Jet, LLC that includes: equity or stocks.

Data availability

Data will be made available on request.

Acknowledgements

The authors would like to thank Dr. Hongtan Liu from the Clean Energy Research Institute of the University of Miami for his valuable discussion on the exergy analysis. We would also like to acknowledge the computing resource provided by the Center for Computational Sciences at the University of Miami.

Disclosure: The University of Miami and Dr. Gecheng Zha may receive royalties for future commercialization of the intellectual property used in this study.

References

[1] K. Xu, G.-C. Zha, Mitigation of serpentine duct flow distortion using coflow jet active flow control, in: AIAA Aviation 2020 Forum, 2020, p. 2954.
[2] K.A. Geiselhart, D.L. Daggett, R. Kawai, D. Friedman, Blended wing body systems studies: boundary layer ingestion inlets with active flow control, NASA Technical Report, NASA/CR-2003-212670, Langley Research Center, Hampton, VA, December 01, 2003.
[3] R.T. Kawai, D.M. Friedman, L. Serrano, Blended wing body (bwb) boundary layer ingestion (bli) inlet configuration and system studies, NASA Technical Report, NASA/CR-2006-214534, Langley Research Center, Hampton, VA, December 01, 2006.
[4] J.D. Mattingly, W.H. Heiser, D.T. Pratt, Aircraft engine design, American Institute of Aeronautics and Astronautics, https://doi.org/10.2514/4.861444, 2002.
[5] D. Miller, G. Addington, Aerodynamic flowfield control technologies for highly integrated airframe propulsion flowpaths, in: 2nd AIAA Flow Control Conference, AIAA 2004-2625, June 2004, 2004.
[6] B. Reichert, B. Wendt, An experimental investigation of s-duct flow control using arrays of low-profile vortex generators, in: 31st Aerospace Sciences Meeting, AIAA 1993-0018, Reno, NV, 11 January 1993 - 14 January, 1993.
[7] B.H. Anderson, J. Gibb, Study on vortex generator flow control for the management of inlet distortion, J. Propuls. Power 9 (3) (1993) 422–430, https://doi.org/10.2514/3.23638.
[8] J. Gibb, M. Jackson, Some preliminary results from tests using vortex generators in the circular/circular diffusing s-duct model m2129 test phase 3, Defense research agency Rept. AP4 (92) WP15.
[9] J. Gibb, B.H. Anderson, Vortex flow control applied to aircraft intake ducts, in: Proceedings of the Royal Aeronautical Society Conf., High Lift and Separation Control, Pape, no. 14, 1995.
[10] B.H. Anderson, J. Gibb, Vortex-generator installation studies on steady-state and dynamic distortion, J. Aircr. 35 (4) (1998) 513–520, https://doi.org/10.2514/2.2340.
[11] A. Jirasek, Design of vortex generator flow control in inlets, J. Aircr. 43 (6) (2006) 1886–1892, https://doi.org/10.2514/1.21364.

[12] J. Yi, C. Kim, B.J. Lee, Adjoint-based design optimization of vortex generator in a s-shaped subsonic inlet, AIAA J. 50 (11) (2012) 2492–2507, https://doi.org/10.2514/1.J051687.
[13] T.J. Burrows, Z. Gong, B. Vukasinovic, A. Glezer, Investigation of trapped vorticity concentrations effected by hybrid actuation in an offset diffuser, in: 54th AIAA Aerospace Sciences Meeting, AIAA 2016-0055, San Diego, California, 2016.
[14] T.J. Burrows, B. Vukasinovic, A. Glezer, Flow dynamics effected by active flow control in an offset diffuser, in: 2018 Flow Control Conference, AIAA 2018-4024, June 25-29, Atlanta, Georgia, 2018.
[15] N.A. Harrison, J. Anderson, J.L. Fleming, W.F. Ng, Active flow control of a boundary layer-ingesting serpentine inlet diffuser, J. Aircr. 50 (1) (2013) 262–271, https://doi.org/10.2514/1.C031818.
[16] I. Rudin, E. Arad, J. Cohen, Performance enhancement of boundary layer ingesting inlet using active flow control methods, in: 2018 Applied Aerodynamics Conference, AIAA 2018-3066, Atlanta, Georgia, June 25–29, 2018.
[17] G.-C. Zha, B.F. Carroll, C.D. Paxton, C.A. Conley, A. Wells, High-performance airfoil using coflow jet flow control, AIAA J. 45 (8) (2007) 2087–2090, https://doi.org/10.2514/1.20926.
[18] A. Lefebvre, B. Dano, W.B. Bartow, M.D. Fronzo, G.-C. Zha, Performance and energy expenditure of coflow jet airfoil with variation of mach number, J. Aircr. 53 (6) (2016) 1757–1767, https://doi.org/10.2514/1.C033113.
[19] G.-C. Zha, W. Gao, C.D. Paxton, Jet effects on co-flow jet airfoil performance, AIAA J. 45 (2007) 1222–1231, https://doi.org/10.2514/1.23995.
[20] G.-C. Zha, C. Paxton, A. Conley, A. Wells, B. Carroll, Effect of injection slot size on high performance co-flow jet airfoil, AIAA J. Aircr. 43 (2006) 987–995, https://doi.org/10.2514/1.37441.
[21] B. Wang, B. Haddoukessouni, J. Levy, G.-C. Zha, Numerical investigations of injection-slot-size effect on the performance of coflow jet airfoils, J. Aircr. 45 (6) (2008) 2084–2091, https://doi.org/10.2514/1.37441.
[22] B. Dano, D. Kirk, G.-C. Zha, Experimental investigation of jet mixing mechanism of co- flow jet airfoil, AIAA-2010-4421, in: 5th AIAA Flow Control Conference, Chicago, IL, 28 Jun - 1 Jul 2010.
[23] B. Dano, G.-C. Zha, M. Castillo, Experimental study of co-flow jet airfoil performance enhancement using discreet jets, in: 49th AIAA Aerospace Sciences Meeting Including the New Horizons Forum and Aerospace Exposition, Orlando, Florida, 04 January 2011 - 07 January 2011, 2011.
[24] A. Lefebvre, G.-C. Zha, Design of high wing loading compact electric airplane utilizing co-flow jet flow control, in: AIAA Paper 2015-0772, AIAA SciTech2015: 53nd Aerospace Sciences Meeting, Kissimmee, FL, 5-9 Jan 2015.
[25] Z. Liu, G.-C. Zha, Transonic Airfoil Performance Enhancement Using Co-Flow Jet Active Flow Control, AIAA Paper 2016-3066, AIAA Aviation, Washington, D.C., June 13-17 2016.
[26] A. Lefebvre, G.-C. Zha, Trade Study of 3D Co-Flow Jet Wing for Cruise and Takeoff/Landing Performance, AIAA Paper 2016-0570, AIAA SCITECH2016, AIAA Aerospace Science Meeting, San Diego, CA, 4-8 January 2016.
[27] G.-C. Zha, Y. Yang, Y. Ren, B. McBreen, Super-lift and thrusting airfoil of coflow jet actuated by micro-compressors, in: 2018 Flow Control Conference, AIAA 2018-3061, Atlanta, Georgia, June 25–29, 2018, 2018.
[28] K. Xu, G.-C. Zha, High control authority three-dimensional aircraft control surfaces using co-flow jet, AIAA J. Aircr. (2020), https://doi.org/10.2514/1.C035727. (Accessed 14 July 2020).
[29] K. Xu, Y. Ren, G.-C. Zha, Numerical analysis of energy expenditure for coflow wall jet separation control, AIAA J. (2022) 1–19, https://doi.org/10.2514/1.J061015.
[30] K. Xu, R. Yan, G.-C. Zha, Numerical investigation of nasa hump using co-flow jet for separation control, in: AIAA Scitech 2020 Forum, Orlando, FL, AIAA 2020-1058, 6-10 January, 2020.
[31] Xu, K. and Ren, Y. and Zha, G.-C., Separation control by co-flow wall jet, AIAA Paper 2020-2954.
[32] K. Xu, G.-c. Zha, Distortion elimination for serpentine inlet using coflow jet flow control with variation of mach numbers, in: AIAA Propulsion and Energy 2020 Forum, 2020, p. 3775.
[33] P.A. Barrios, Y. Ren, K. Xu, G.-C. Zha, Design of 3d co-flow jet airfoil with integrated micro-compressor for high operating efficiency at cruise condition, in: AIAA Aviation 2021, Washington, D.C., AIAA 2021-2581, 7-11 June 2021.
[34] K. Xu, G.-C. Zha, Design of high specific speed mixed flow micro-compressor for co-flow jet actuators, in: GT2019-90980, IGTI Turbo Expo 2019, Phoenix, June 17 - 21, 2019, 2019.
[35] P. Patel, G.-C. Zha, Micro-compressor casing treatment using non-matching mesh interface, in: ASME Turbo Expo 2019 Turbomachinery Technical Conference and Exposition, GT2019-90977, American Society of Mechanical Engineers, 2019.
[36] Y. Wang, G.-C. Zha, Study of 3D Co-flow Jet Wing Induced Drag and Power Consumption at Cruise Conditions, AIAA Paper 2019-0034, AIAA SciTech 2019, San Diego, CA, January 7-11, 2019.
[37] Y. Wang, G.-C. Zha, Study of super-lift coefficient of co-flow jet airfoil and its power consumption, in: AIAA Aviation 2019 Forum, 2019, p. 3652.
[38] J. Seddon, E.L. Goldsmith, Intake Aerodynamics, AIAA Inc., New York, 1985.
[39] C. Reid, The Response of Axial Flow Compressors to Intake Flow Distortion, Vol. 79832, American Society of Mechanical Engineers, 1969.
[40] Advisory Group for Aerospace Research and Development, Air intakes for high speed vehicles, Fluid Dynamics Panel Working Group 13, AR-270, Fort Worth, TX, (Sep 1991).
[41] A.C. Willmer, T.W. Brown, E.L. Goldsmith, Effects of intake geometry on circular pitot intake performance at zero and low forward speeds, Aerodynamics of Power Plant Installation, AGARD CP301, Paper 5, Toulouse, France (May, 1981).
[42] P.R. Spalart, S.R. Allmaras, A one-equation turbulence model for aerodynamic flows, AIAA-92-0439, in: 30th Aerospace Sciences Meeting and Exhibit, Reno, NV, U.S.A., 06 January 1992 - 09 January 1992, 1992.
[43] Y. Shen, G.-C. Zha, B. Wang, Improvement of stability and accuracy for weighted essentially nonoscillatory scheme, AIAA J. 47 (2009) 331–344, https://doi.org/10.2514/1.37697.
[44] Y. Shen, G.-C. Zha, X. Chen, High order conservative differencing for viscous terms and the application to vortex-induced vibration flows, J. Comput. Phys. 228 (2) (2009) 8283–8300, https://doi.org/10.1016/j.jcp.2009.08.004.
[45] Y. Shen, G.-C. Zha, Improvement of the weno scheme smoothness estimator, Int. J. Numer. Methods Fluids 64 (6) (2010) 653–675, https://doi.org/10.1002/fld.2168.
[46] G.-C. Zha, Y. Shen, B. Wang, An improved low diffusion E-CUSP upwind scheme, J. Comput. Fluids 48 (2011) 214–220, https://doi.org/10.1016/j.compfluid.2011.03.012.
[47] G-C. Zha, E. Bilgen, Numerical solutions of euler equations by using a new flux vector splitting scheme, Int. J. Numer. Methods Fluids 17 (2) (1993) 115–144, https://doi.org/10.1002/fld.1650170203.
[48] G.-C. Zha, E. Bilgen, Numerical study of three-dimensional flows using unfactored upwind-relaxation sweeping algorithm, J. Comput. Phys. 125 (2) (1996) 425–433, https://doi.org/10.1006/jcph.1996.0104.
[49] B. Wang, Z. Hu, G.-C. Zha, General subdomain boundary mapping procedure for structured grid implicit cfd parallel computation, J. Aerosp. Comput. Inf. Commun. 5 (11) (2008) 425–447, https://doi.org/10.2514/1.35498.
[50] Y. Yang, G.-C. Zha, Super-Lift Coefficient of Active Flow Control Airfoil: What is the Limit? AIAA SCITECH2017, 55th AIAA Aerospace Science Meeting, Grapevine, Texas.
[51] J. Dudek, S-duct inlet with and without vortex generator validation cases, NPARC alliance verification and validation archive, https://www.grc.nasa.gov/WWW/wind/valid/sduct/sduct.html, 02 Mar 2009.
[52] O. Nesrin, H. Geoffrey, Thermopedia, Begell House, 2005.